PHYSICAL REVIEW D **93,** 095027 (2016)

Di-Higgs decay of stoponium at a future photon-photon collider

Hayato Ito, Takeo Moroi, and Yoshitaro Takaesu
Department of Physics, University of Tokyo, Tokyo 113-0033, Japan
(Received 20 February 2016; published 31 May 2016)

We study the detectability of the stoponium in the di-Higgs decay mode at the photon-photon collider option of the International e^+e^- Linear Collider, the center-of-mass energy of which is planned to reach ∼1 TeV. We find that 5σ detection of the di-Higgs decay mode is possible with the integrated electron-beam luminosity of 1 ab^{-1} if the signal cross section, $\sigma(\gamma\gamma \to \sigma_{\tilde{t}_1} \to hh)$, of $\mathcal{O}(0.1)$ fb is realized for the stoponium mass smaller than ∼800 GeV at 1 TeV ILC. Such a value of the cross section can be realized in the minimal supersymmetric standard model with relatively large trilinear stop-stop-Higgs coupling constant. The implication of the stoponium cross section measurement for the minimal supersymmetric standard model stop sector is also discussed.

DOI: 10.1103/PhysRevD.93.095027

I. INTRODUCTION

Low-energy supersymmetry (SUSY) is an attractive candidate of the physics beyond the standard model even though the recent LHC experiment is imposing stringent constraints on the mass scale of superparticles. Importantly, there is still a possibility that there exist superparticles with their masses below the TeV scale. In particular, a scalar top-quark (stop) with the mass of $\mathcal{O}(100)$ GeV is still allowed if there exists a neutralino of which the mass is just below that of the stop mass; in such a case, even if the stop is produced at the LHC experiments, its decay products are too soft to be observed so that it can evade the detection at the LHC.

If there exists a stop with a mass of $\mathcal{O}(100)$ GeV, it will become an important target of future collider experiments. If the signal of the stop is discovered at the LHC, the LHC and the International e^+e^- Linear Collider (ILC) may play an important role in studying its basic properties (like the mass and left-right mixing angle). It is, however, also important to study the strength of the stop-stop-Higgs coupling because the Higgs mass in the supersymmetric model is sensitive to it; measurement of the stop-stop-Higgs coupling is crucial to understanding the origin of the Higgs mass in the supersymmetric model. It motivates the study of the stop-stop bound state (so-called stoponium, which is denoted as $\sigma_{\tilde{t}_1}$ in this paper) because the decay rate of the stoponium crucially depends on such a coupling. If we observe the process of $\sigma_{\tilde{t}_1} \to hh$, we can acquire information about the stop-stop-Higgs coupling.

Photon-photon colliders may be useful to perform such a study [1,2].[1] A photon-photon collider is one of the options of the ILC and can be realized by converting a high-energy electron (or positron) beam of the ILC to the backscattered high-energy photon. One of the advantages of photon-photon colliders is that the single production of some scalar particles (including the Higgs boson) is possible so that the kinematical reach is close to the total center-of-mass energy; this is a big contrast to other colliders with pp and e^+e^- collision. The single production of the stoponium bound state is also possible with the photon-photon collision, and hence it is interesting to consider the stoponium study at the photon-photon collider.

In this paper, we investigate how and how well we can study the property of the stoponium at the photon-photon collider, paying particular attention to the process of $\gamma\gamma \to \sigma_{\tilde{t}_1} \to hh$. We calculate the cross section of the stoponium production process at the photon-photon collider. We also estimate backgrounds and discuss the possibility of observing the stoponium production process at the photon-photon collider. Implication of the cross section measurement of the stoponium di-Higgs decay mode for the minimal supersymmetric standard model (MSSM) stop sector is also discussed.

The organization of this paper is as follows. In Sec. II, we discuss the theoretical framework of the stoponium and its production cross section and decay widths at the photon-photon collider. The detectability of the stoponium in the di-Higgs decay mode is investigated in Sec. III. In Sec. IV, we discuss the implication of the cross section measurement of the stoponium production and di-Higgs decay for the MSSM stop sector. Then, we provide our summary in Sec. V.

II. STOPONIUM: BASIC PROPERTIES

A. Framework

Let us first summarize the framework of our analysis. We assume the MSSM as the underlying theory. The relevant part of the superpotential for our study is given by

$$W = y_t \epsilon_{ij} \hat{\bar{t}}_R \hat{Q}_L^i \hat{H}_u^j + \mu \epsilon_{ij} \hat{H}_u^i \hat{H}_d^j, \tag{1}$$

[1]For the stoponium studies at other colliders, see Refs. [3–18].

where y_t is the top Yukawa coupling; H_u, H_d, t_R and Q_L denote up- and down-type Higgses, right-handed top quark, and third-generation quark-doublet, respectively; and a hat is used for the corresponding superfields. In addition, i and j are $SU(2)_L$ indices, while the color indices are omitted for simplicity. The relevant part of the soft SUSY breaking terms is

$$\mathcal{L}_{\rm soft} = -m_{\tilde{t}_R}^2 |\tilde{\bar{t}}_R|^2 - m_{\tilde{Q}_L}^2 |\tilde{Q}_L|^2 + y_t A_t (\epsilon_{ij} \tilde{\bar{t}}_R \tilde{Q}_L^i H_u^j + \text{H.c.}), \tag{2}$$

where a tilde is used for superpartners.

Neglecting the effects of flavor mixing, the stop mass terms are expressed as

$$\mathcal{L}_{\rm mass} = -(\tilde{t}_L^*, \tilde{t}_R^*) \begin{pmatrix} m_{\tilde{Q}_L}^2 + m_t^2 + D_L & -m_t X_t \\ -m_t X_t & m_{\tilde{t}_R}^2 + m_t^2 + D_R \end{pmatrix} \times \begin{pmatrix} \tilde{t}_L \\ \tilde{t}_R \end{pmatrix}, \tag{3}$$

where m_t is the top-quark mass, $\tilde{t}_R \equiv \tilde{\bar{t}}_R^*$,

$$X_t \equiv A_t + \mu \cot\beta, \tag{4}$$

and

$$D_L \equiv m_Z^2 \cos 2\beta \left(\frac{1}{2} - \frac{2}{3} \sin^2\theta_{\rm W} \right), \tag{5}$$

$$D_R \equiv m_Z^2 \cos 2\beta \left(\frac{2}{3} \sin^2\theta_{\rm W} \right), \tag{6}$$

with $\theta_{\rm W}$ being the Weinberg angle, m_Z the Z-boson mass, and $\tan\beta \equiv \langle H_u^0 \rangle / \langle H_d^0 \rangle$. The A_t and μ parameters are taken to be real. The mass eigenstates are given by the linear combination of the left- and right-handed stops; we define the mixing angle $\theta_{\tilde{t}}$ as

$$\begin{pmatrix} \tilde{t}_1 \\ \tilde{t}_2 \end{pmatrix} = \begin{pmatrix} \cos\theta_{\tilde{t}} & \sin\theta_{\tilde{t}} \\ -\sin\theta_{\tilde{t}} & \cos\theta_{\tilde{t}} \end{pmatrix} \begin{pmatrix} \tilde{t}_L \\ \tilde{t}_R \end{pmatrix}, \tag{7}$$

where $\tilde{t}_1$ and $\tilde{t}_2$ are lighter and heavier mass eigenstates with the masses of $m_{\tilde{t}_1}$ and $m_{\tilde{t}_2}$, respectively.

Before closing this subsection, we comment on the lightest MSSM Higgs boson mass. The lightest Higgs mass is sensitive to the masses of stops as well as to the A_t parameter through radiative corrections. With the stop masses being fixed, the lightest Higgs mass becomes equal to the observed Higgs mass (which is taken to be $m_h \simeq 125.7$ GeV throughout our study) for four different values of A_t; two of them are positive, and the others are negative. We call these as positive-large, positive-small, negative-large, and negative-small solutions of A_t, where large and small solutions correspond to those with large and small values of $|A_t|$.

B. Stoponium production at a photon-photon collider and its decay

Because of the strong interaction, a stop and an antistop can form a bound state, called stoponium. In this analysis, we concentrate on the case where the decay rate of a stop is negligibly small. Because we are interested in the collider study of the stoponium, we concentrate on the bound state of the lighter stop. The lowest bound state, $\sigma_{\tilde{t}_1}$, has the quantum number of $J^{PC} = 0^{++}$, and hence its resonance production does not occur at e^+e^- colliders. At photon-photon colliders, on the contrary, the process $\gamma\gamma \to \sigma_{\tilde{t}_1} \to F$ may occur, where F denotes final-state particles of the stoponium decay. High-energy photon-photon collisions can be achieved by photons originating from backscattered lasers off electron beams, and this possibility was discussed in detail [19,20]. For a concrete discussion, we assume a photon-photon collider utilizing an upgraded ILC, the energy of which is planned to reach $\sqrt{s_{ee}} = 1$ TeV [21].

With the c.m. energy of colliding photons, $\sqrt{s_{\gamma\gamma}}$, being fixed,[2] the cross section for the process $\gamma\gamma \to \sigma_{\tilde{t}_1} \to F$ can be written as [20]

$$\hat{\sigma}(\gamma\gamma \to \sigma_{\tilde{t}_1} \to F; s_{\gamma\gamma}) = \left(\frac{1 + \xi_2 \xi_2'}{2} \right) \hat{\sigma}_{++}(\gamma\gamma \to \sigma_{\tilde{t}_1} \to F; s_{\gamma\gamma}). \tag{8}$$

Here, ξ_2 and ξ_2' are the Stokes parameters of the initial-state photons where $\xi_2 = \pm 1$ corresponds to the photons with helicity ± 1. In this study, we only consider axially symmetric electron beams, and other components of the Stokes parameters ($\xi_{1,3}$) are negligible [20]. In addition, $\hat{\sigma}_{++}$ ($= \hat{\sigma}_{--}$) is the cross section for photon collisions with circular polarization. In the following, we assume that the decay width of the stop is much smaller than the total decay width of the stoponium (and hence is smaller than the stop mass). This is the case when the mass difference between the lighter stop and the lightest supersymmetric particle (LSP), which is assumed to be the lightest neutralino in our analysis, is small enough. Furthermore, as we see below, we will consider the sample points at which the decay width of the stoponium is much smaller than the splittings of the energy levels of bound states. The cross section $\hat{\sigma}_{++}$ is given with the Breight-Wigner approximation by

[2] In this article, we denote the center-of-mass energy of colliding photons by $\sqrt{s_{\gamma\gamma}}$ and that of colliding electrons and positrons by $\sqrt{s_{ee}}$.

$$\hat{\sigma}_{\lambda\lambda'}(\gamma\gamma \to \sigma_{\tilde{t}_1} \to F; s_{\gamma\gamma}) = \frac{16\pi m_\sigma^2}{s_{\gamma\gamma}} \frac{\Gamma(\sigma_{\tilde{t}_1} \to \gamma\gamma)\Gamma(\sigma_{\tilde{t}_1} \to F)}{(s_{\gamma\gamma} - m_\sigma^2)^2 + m_\sigma^2\Gamma_\sigma^2} \delta_{\lambda\lambda'}, \quad (9)$$

where Γ_σ and $\Gamma(\sigma_{\tilde{t}_1} \to \gamma\gamma/F)$ are the total and partial decay widths of the stoponium, respectively; $\lambda = \pm$ and $\lambda' = \pm$ are polarizations of initial-state photons; and m_σ is the mass of the stoponium, which is roughly estimated as

$$m_\sigma = 2m_{\tilde{t}_1}, \quad (10)$$

throughout this paper. Detailed calculations in Ref. [22] show that the error of this estimation is ~0.5% and negligible for our discussion.

Since backscattered photons off electron beams are not monochromatic, the cross section at the photon-photon collider is given by[3]

$$\sigma(\gamma\gamma \to \sigma_{\tilde{t}_1} \to F; s_{ee}) = \frac{1}{L_{ee}} \int_0^{y_m} dy dy' \frac{d^2L_{\gamma\gamma}}{dy dy'} \hat{\sigma}(\gamma\gamma \to \sigma_{\tilde{t}_1} \to F; s_{\gamma\gamma} = yy' s_{ee}), \quad (11)$$

using the luminosity function of backscattered photons [19,20,23] denoted by $d^2L_{\gamma\gamma}/dydy'$ (with y and y' being the photon energies normalized by the energy of the electron beam E_e in the laboratory frame).[4] Here, $y_m \equiv x/(x+1), x \equiv 4E_e\omega_0/m_e^2$ with ω_0 being the averaged energy of the laser photons in a laboratory frame, and L_{ee} and $s_{ee}(= 4E_e^2)$ are the luminosity and c.m. energy of the electron beams, respectively. We take $x = 4.8$ to maximize y_m without spoiling the photon luminosity [23]. Since we consider the case where $\Gamma_\sigma \sim \mathcal{O}(10^{-3})$ GeV $\ll m_\sigma$, we use the narrow-width approximation and obtain

$$\sigma(\gamma\gamma \to \sigma_{\tilde{t}_1} \to F; s_{ee}) \simeq \frac{16\pi^2\Gamma(\sigma_{\tilde{t}_1} \to \gamma\gamma)}{m_\sigma} \mathrm{Br}(\sigma_{\tilde{t}_1} \to F) \times \frac{1}{s_{ee}L_{ee}} \int_{z_0^2/y_m}^{y_m} \frac{dy}{y} \left[\frac{d^2L_{\gamma\gamma}}{dydy'} \frac{1 \pm \xi_2(y)\xi_2(y')}{2}\right]_{y'=z_0^2/y}, \quad (12)$$

with $z_0 = m_\sigma/\sqrt{s_{ee}}$. The y dependence of ξ_2 is given by [19,20]

$$\xi_2(y) = \frac{C_{20}(x,y)}{C_{00}(x,y)}, \quad (13)$$

where

$$C_{00}(x,y) = \frac{1}{1-y} - y + (2r-1)^2 - \lambda_e P_l x r (2r-1)(2-y), \quad (14)$$

$$C_{20}(x,y) = \lambda_e r x[1 + (1-y)(2r-1)^2] - P_l(2r-1)\left(\frac{1}{1-y} + 1 - y\right), \quad (15)$$

with $\lambda_e/2$ and P_l being the mean helicities of initial electrons and laser photons, respectively, and $r = y/x(1-y)$. In our numerical calculation, we take $\lambda_e = 0.85$ and $P_l = -1$.

The decay rates of the stoponium are related to the matrix elements for the pair-annihilation processes of the stop and antistop. For the case of two-body final states, i.e., $\sigma_{\tilde{t}_1} \to ff'$, the decay width is related to the matrix element of the scattering process $\mathcal{M}(\tilde{t}_1\tilde{t}_1^* \to ff')$ as [6]

$$\Gamma(\sigma_{\tilde{t}_1} \to ff') = \frac{3}{32\pi^2(1+\delta_{ff'})} \beta_{ff'} \frac{|R_{1S}(0)|^2}{m_\sigma^2} \times \sum_{\text{spin, color}} |\mathcal{M}(\tilde{t}_1\tilde{t}_1^* \to ff')|^2_{v\to 0}, \quad (16)$$

where

$$\beta_{ff'}^2 = \left(1 - \frac{m_f^2}{m_\sigma^2} - \frac{m_{f'}^2}{m_\sigma^2}\right)^2 - 4\frac{m_f^2}{m_\sigma^2}\frac{m_{f'}^2}{m_\sigma^2}, \quad (17)$$

v is the velocity of the stops in the initial state, and $R_{1S}(0)$ is the stoponium radial wave function at $r = 0$ (with r being the distance between $\tilde{t}_1$ and $\tilde{t}_1^*$). In our study, we use [6,9,22]

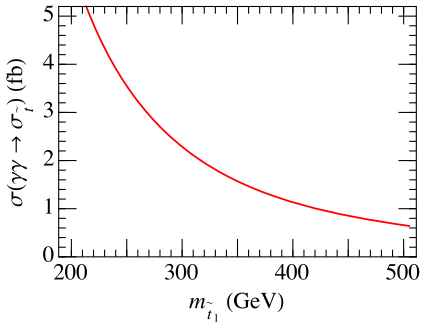

FIG. 1. The stoponium production cross section $\sigma(\gamma\gamma \to \sigma_{\tilde{t}_1})$ as a function of the lightest stop mass $m_{\tilde{t}_1}$. The center-of-mass energy of the electron beams is taken to be $\sqrt{s_{ee}} = 1.26m_\sigma$, which maximizes the cross section.

[3]In this article, we define cross sections for the photon-photon collider as the number of events normalized by the luminosity of electron beams, L_{ee}.

[4]For more details about the luminosity function, see Appendix A.

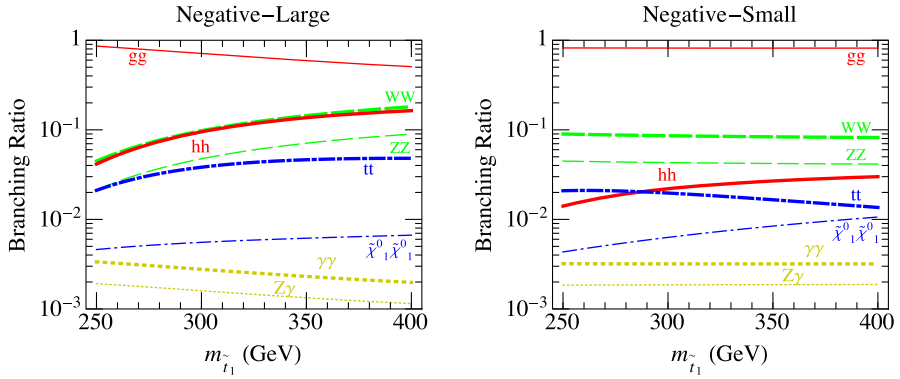

FIG. 2. The branching ratios of the stoponium as functions of the lightest stop mass, taking $m_{\tilde{t}_2} = 4$ TeV, $m_{\tilde{\chi}^0_1} = m_{\tilde{t}_1} - 50$ GeV, $\tan\beta = 10$, $\mu = 2$ TeV with negative-large (left) and negative-small (right) solutions of the A_t, which give $m_h = 125.7$ GeV.

$$\frac{|R_{1S}(0)|^2}{m_\sigma^2} = 0.1290 + 0.0754L + 0.0199L^2 + 0.0010L^3 \text{ [GeV]}, \tag{18}$$

where $L = \ln(m_{\tilde{t}_1}/250\text{ GeV})$. The matrix elements for the stop pair-annihilation processes relevant to our study are summarized in Appendix B.

In Fig. 1, we plot the stoponium production cross section

$$\sigma(\gamma\gamma \to \sigma_{\tilde{t}_1}) = \frac{16\pi^2\Gamma(\sigma_{\tilde{t}_1} \to \gamma\gamma)}{m_\sigma}\frac{1}{s_{ee}L_{ee}}\int_{z_0^2/y_m}^{y_m}\frac{dy}{y} \times \left[\frac{d^2L_{\gamma\gamma}}{dydy'}\frac{1 \pm \xi_2(y)\xi_2(y')}{2}\right]_{y'=z_0^2/y}, \tag{19}$$

taking $\sqrt{s_{ee}} = 1.26 m_\sigma$, which maximizes the cross section. The stoponium production cross section can be as large as $O(1)$ fb for $m_{\tilde{t}_1} \lesssim 500$ GeV.

In Fig. 2, we show the branching ratios of the stoponium as functions of the lightest stop mass, taking $m_{\tilde{t}_2} = 4$ TeV, $m_{\tilde{\chi}^0_1} = m_{\tilde{t}_1} - 50$ GeV, $\tan\beta = 10$, $\mu = 2$ TeV, and negative-large or negative-small solutions of the A_t parameter. The positive A_t solutions give similar branching ratios. The gg decay mode dominates the stoponium decay, and this may be a useful mode for stoponium searches at photon-photon colliders. However, the gg branching ratio is completely determined by the strong coupling constant, and measuring this mode does not give much information on SUSY interactions. Therefore, we do not investigate this mode in this study. Although WW and ZZ decay modes have non-negligible branching ratios of $\mathcal{O}(1-10)\%$, they suffer from large SM backgrounds [1,2,24]. We therefore investigate the hh decay mode in the following sections as a probe to the SUSY interactions, especially to the stop sector. We will see in the next section that the signal-to-background ratio of the $\gamma\gamma \to \sigma_{\tilde{t}_1} \to hh$ process may be large enough to be observed at the ILC-based photon-photon collider.

III. $\sigma_{\tilde{t}_1} \to hh$ SEARCH AT A PHOTON-PHOTON COLLIDER

In this section, we discuss a search strategy for the hh decay mode of the stoponium at the photon-photon collider. We assume an upgraded ILC, the energy of which is planned to reach $\sqrt{s_{ee}} = 1$ TeV [21] with the integrated luminosity of $\mathcal{L}_{ee} \sim 1$ ab^{-1}.

For our numerical calculation, we adopt four sample SUSY model points with $m_{\tilde{t}_1} = 250$, 300, 350, and 400 GeV as summarized in Table I. We assume that the lighter stop and the lightest neutralino, $\tilde{\chi}^0_1$, will be discovered before the photon-photon collider experiment is carried out. In addition, if the stop is within the kinematical reach of the photon-photon collider, detailed studies of the stop will have been already performed with the e^+e^- collisions at the ILC, and hence we also assume that the basic properties of the lighter stop such as the mass and the chirality will be measured at the ILC before the start of the photon-photon collider. We consider the cases where the bino is the LSP with $m_{\tilde{\chi}^0_1} = 150$, 250, 300, and 350 GeV for each $m_{\tilde{t}_1}$, respectively.[5] Other SUSY particles are assumed to be sufficiently heavy ($\gtrsim$2 TeV) and irrelevant to our photon collider study. $\tan\beta$ and the μ parameter are taken to be 10 and 2 TeV, respectively, for all the sample points, and the Higgs mass of 125.7 GeV is realized by adjusting the A_t parameter and the heavier stop mass, $m_{\tilde{t}_2}$. (For our numerical calculation of the Higgs mass, we use `FeynHiggs v2.11.3` [25–29].) To maximize the stoponium production cross section, we adjust the c.m. energy of the electron beams as $\sqrt{s_{ee}} \sim 1.26 m_\sigma$ for each sample point shown in Table I. The cross sections of the process $\gamma\gamma \to \sigma_{\tilde{t}_1} \to hh$ for those sample points are also shown in the table.

Before starting the main subject of this section, we comment that, in our sample points, the decay width of the

[5]We do not consider the relic abundance of the LSP in this study.

TABLE I. The sample SUSY models we adopt in our collider analyses. All the SUSY parameters are given in units of GeV. We take $\tan\beta = 10$ and $\mu = 2$ TeV in all the sample points. Other SUSY particle masses and soft-breaking trilinear couplings are taken to be 2 TeV. These sample points realize $m_h = 125.7$ GeV. The employed c.m. energy of the electron beams and the cross section of the $\gamma\gamma \to \sigma_{\tilde{t}_1} \to hh$ process are also shown for each sample point.

	Point 1	Point 2	Point 3	Point 4
$m_{\tilde{t}_1}$	250	300	350	400
$m_{\tilde{t}_2}$	3480	3810	4110	4080
A_t	−4370	−4940	−5460	−5670
$m_{\tilde{\chi}_1^0}$	150	250	300	350
$\sqrt{s_{ee}}$ [GeV]	625	750	875	1000
$\sigma(\gamma\gamma \to \sigma_{\tilde{t}_1} \to hh)$ [fb]	0.34	0.26	0.2	0.18
Γ_σ [MeV]	3.2	4.0	4.7	6.0

stoponium is much smaller than the splitting of the energy levels of bound states. The decay width of the stoponium is also shown in Table I and is $\mathcal{O}(1)$ MeV. On the contrary, the energy splittings of the bound states are typically of the order of $\sim\alpha_s^2 m_{\tilde{t}_1}$ (with α_s being the strong coupling constant), which is a few GeV in our sample points. Furthermore, as we mentioned, we assume that the decay width of the stop is much smaller than the total decay width of the stoponium, adopting the mass degeneracy between the stop and the LSP. Thus, the formation criteria of the bound states discussed in Refs. [30–32] are satisfied in the sample points we adopted.

A. Signal event selection

From Table I, we see that the cross sections $\sigma(\gamma\gamma \to \sigma_{\tilde{t}_1} \to hh)$ for the sample points are of $\mathcal{O}(0.1)$ fb, and then the process would give only $\mathcal{O}(100)$ events at 1 ab^{-1}. Therefore, we use the main $b\bar{b}$ decay mode of the Higgs boson for the signal process, i.e., $\gamma\gamma \to \sigma_{\tilde{t}_1} \to hh \to b\bar{b}b\bar{b}$.

To simulate the signal process, we generate events where a scalar particle (which corresponds to the stoponium) is produced at the photon-photon collider and decayed to a Higgs pair with their subsequent decays to $b\bar{b}$, using `MadGraph5_aMC@NLO v2` [33]; the luminosity function of the colliding photons [20,23] is implemented by modifying the electron structure function routines in `MadGraph5`. The cross section of the events is normalized to that of the signal process according to Eq. (12). The generated events are then showered with `PYTHIA v6.4` [34] and passed to `DELPHES v3` [35] for fast detector simulations. In the detector simulation, we assume energy resolutions of $2\%/\sqrt{E(\mathrm{GeV})} \oplus 0.5\%$ and $50\%/\sqrt{E(\mathrm{GeV})} \oplus 3\%$ for an electromagnetic calorimeter and hadron calorimeter, respectively, based on the ILC Technical Design Report (TDR) [36]. `FastJet v3` [37] is employed for jet clustering using the anti-k_t algorithm [38] with the distance parameter of 0.5.

From the generated events, we first select events containing more than four jets and satisfying $p_T > 30$ GeV and $|\eta| < 2.0$ for all of the four highest p_T jets (preselection), where p_T and η are the transverse momentum and pseudorapidity, respectively. We then impose the following cuts successively:

S1: $m_\sigma - 60\ \mathrm{GeV} \le M_{4\,\mathrm{jets}} \le m_\sigma + 40\ \mathrm{GeV}$.

S2: $N_{b\text{-tag}} \ge 3$.

S3: $105.7\ \mathrm{GeV} \le M_1 \le 130.7\ \mathrm{GeV}$,
$100.7(105.7)\ \mathrm{GeV} \le M_2 \le 130.7\ \mathrm{GeV}$
(for the Point 1 $(2,3,4)$).

S4: $\min\{\Delta R_1, \Delta R_2\} \le 1.4$,
$\max\{\Delta R_1, \Delta R_2\} \le 1.8$.

Here, $M_{4\,\mathrm{jets}}$ is the invariant mass of the four highest p_T jets. $N_{b\text{-tag}}$ is the number of b-tagged jets in each event, where we assume 80% b-tag efficiency and 10% and 0.1% mistag rates for c jets and u, d, s jets, respectively. In S3 and S4, $M_{1(2)}$ and $\Delta R_{1(2)}$ are defined as follows. We first divide the leading four jets into two jet pairs. Among three possible pairings, we choose the one which minimizes $(M_1 - m_h)^2 + (M_2 - m_h)^2$, where M_1 and M_2 are the invariant masses of the jet pairs such that

$$|M_1 - m_h| < |M_2 - m_h|. \tag{20}$$

$\Delta R_{1(2)}$ is defined as

$$\Delta R_{1(2)} = \sqrt{(\Delta\eta_{1(2)})^2 + (\Delta\phi_{1(2)})^2}, \tag{21}$$

where $\Delta\eta_i$ and $\Delta\phi_i (i = 1, 2)$ are respectively pseudorapidity and azimuthal angle differences between the paired jets whose invariant mass is M_i.

B. Backgrounds

After imposing the selection cuts, the relevant background processes are the nonresonant hh, $bb\bar{b}\,\bar{b}$, $b\bar{b}c\bar{c}$, $cc\bar{c}\,\bar{c}$, $b\bar{b}q\bar{q}$ (where $q = u$, d, s), $t\bar{t}$, ZZ, W^+W^-, and W^+W^-Z production processes. The event numbers after all the selection cuts are imposed are estimated for the above background processes as in the signal process case, except the nonresonant hh and ZZ backgrounds, which are loop-induced processes.

As for hh and ZZ backgrounds, we use approximate estimations; the event numbers of the nonresonant hh background after each cut are estimated with ∼15% uncertainty, and the event numbers of the ZZ background are estimated as the upper bounds after all cuts are applied.

We will see in Sec. III C that even these rough estimations are enough for our study and leave more detailed estimations for future works.

In the following, we describe our procedure to estimate the nonresonant hh and ZZ backgrounds. The production cross sections of background processes at the photon-photon collider can be expressed in the similar way as for the signal process discussed in Sec. II B,

$$\begin{aligned}&\sigma(\gamma\gamma\to F;s_{ee})\\&=\frac{1}{L_{ee}}\int_0^{y_m}dydy'\frac{d^2L_{\gamma\gamma}}{dydy'}\hat{\sigma}(\gamma\gamma\to F;s_{\gamma\gamma}=yy's_{ee})\\&=\sum_{\lambda\lambda'=++,+-}\int_0^{y_m}dz\left[\frac{1}{L_{ee}}\frac{dL_{\gamma\gamma}}{dz}\frac{1\pm\xi_2\xi_2'}{2}\right]\\&\quad\times(z)\hat{\sigma}_{\lambda\lambda'}(\gamma\gamma\to F;s_{\gamma\gamma}=z^2s_{ee}),\end{aligned}\tag{22}$$

where

$$\begin{aligned}&\left[\frac{1}{L_{ee}}\frac{dL_{\gamma\gamma}}{dz}\frac{1\pm\xi_2\xi_2'}{2}\right](z)\\&\equiv 2z\int_{z^2/y_m}^{y_m}\frac{dy}{y}\frac{1}{L_{ee}}\frac{d^2L_{\gamma\gamma}}{dydy'}\frac{1\pm\xi_2(y)\xi_2(y')}{2}\bigg|_{y'=z^2/y},\end{aligned}\tag{23}$$

with $z=\sqrt{s_{\gamma\gamma}/s_{ee}}$. In the second line, contributions from ξ_1 and ξ_3 are negligible since we consider axial symmetric electron beams; the sign in front of the stokes parameters is taken to be positive (negative) for $\lambda\lambda'=++(+-)$.

1. $\gamma\gamma\to hh\to bb\bar{b}\,\bar{b}$

First, let us discuss the nonresonant Higgs pair production process. The dominant background contributions are from Higgs pairs decaying to bottom quarks. Based on Eq. (22), the cross section after all selection cuts are imposed, $\sigma_{\rm cut}(\gamma\gamma\to hh\to bb\bar{b}\,\bar{b};s_{ee})$, is given by

$$\begin{aligned}&\sigma_{\rm cut}(\gamma\gamma\to hh\to bb\bar{b}\,\bar{b})\\&=\mathrm{Br}(h\to b\bar{b})^2\sum_{\lambda\lambda'=++,+-}\int_0^{y_m}dz\\&\quad\times\int_{z^2/y_m}^{y_m}dy\frac{1}{L_{ee}}\frac{d^2L_{\gamma\gamma}}{dzdy}\left(\frac{1\pm\xi_2\xi_2'}{2}\right)\\&\quad\times\int_0^1 d\cos\theta^*\frac{d\hat{\sigma}_{\lambda\lambda'}(\gamma\gamma\to hh;s_{\gamma\gamma}=z^2s_{ee},\theta^*)}{d\cos\theta^*}\\&\quad\times\varepsilon_{\lambda\lambda'}(z,y,\theta^*),\end{aligned}\tag{24}$$

where $\varepsilon_{\lambda\lambda'}(z,y,\theta^*)$ is the total efficiency of all the selection cuts for events with a c.m. energy $\sqrt{s_{\gamma\gamma}}=z\sqrt{s_{ee}}$, a total energy measured in the laboratory frame $E_{\rm lab}=(y+z^2/y)E_{ee}$, and Higgs scattering angle θ^* in the c.m. frame of the γ-γ collision.

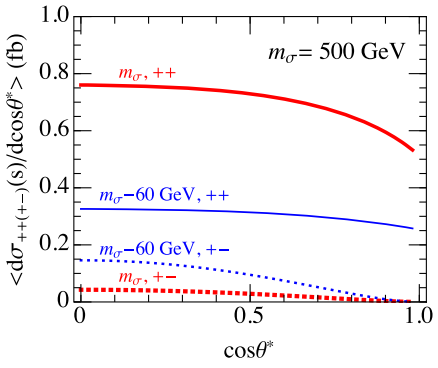

FIG. 3. The angular distributions of the luminosity-weighted cross sections evaluated at $\sqrt{s_{\gamma\gamma}}=m_\sigma$ (thick red lines) and $m_\sigma-60$ GeV (thin blue lines) for the $m_\sigma=500$ GeV ($\sqrt{s_{ee}}=625$ GeV) case. The solid and dashed lines represent $(++)$ and $(+-)$ helicity configurations of initial photons, respectively.

We approximate this expression by neglecting the angular dependence of the Higgs production cross section. In Fig. 3, we plot the luminosity-weighted differential cross section

$$\begin{aligned}&\left\langle\frac{d\hat{\sigma}_{\lambda\lambda'}(\gamma\gamma\to hh,s_{\gamma\gamma},\theta^*)}{d\cos\theta^*}\right\rangle\\&\equiv\frac{d\hat{\sigma}_{\lambda\lambda'}(\gamma\gamma\to hh;s_{\gamma\gamma},\theta^*)}{d\cos\theta^*}\left[\frac{1}{L_{ee}}\frac{dL_{\gamma\gamma}}{dz}\frac{1\pm\xi_2\xi_2'}{2}\right]\\&\quad\times(z=\sqrt{s_{\gamma\gamma}/s_{ee}}),\end{aligned}\tag{25}$$

for $\sqrt{s_{\gamma\gamma}}=m_\sigma$ and $m_\sigma-60$ GeV with $m_\sigma=500$ GeV (Point 1). In evaluating the differential cross section $d\hat{\sigma}_{\lambda\lambda'}(\gamma\gamma\to hh;s_{\gamma\gamma},\theta^*)/d\cos\theta^*$, we use the one-loop expressions given by Ref. [39].

From the figure, we see that the luminosity-weighted differential cross sections for the $(++)$ photon helicity are larger than those for the $(+-)$ photon helicity. Those cross sections do not change significantly over the whole range of $\cos\theta^*$ for both $\sqrt{s_{\gamma\gamma}}$ choices. We have also checked that Point 4 shows a similar behavior with $\sqrt{s_{\gamma\gamma}}=800$ GeV. Therefore, we approximate that Higgs pairs are produced almost isotropically in the c.m. frame of the photon collision. Then, Eq. (24) is written as

$$\begin{aligned}&\sigma_{\rm cut}(\gamma\gamma\to hh\to bb\bar{b}\,\bar{b};s_{ee})\\&\simeq\mathrm{Br}(h\to b\bar{b})^2\sum_{\lambda\lambda'=++,+-}\int_0^{y_m}dz\\&\quad\times\left[\frac{1}{L_{ee}}\frac{dL_{\gamma\gamma}}{dz}\left(\frac{1\pm\xi_2\xi_2'}{2}\right)\varepsilon_{\lambda\lambda'}\right](z)\\&\quad\times\frac{d\hat{\sigma}_{\lambda\lambda'}(\gamma\gamma\to hh;s_{\gamma\gamma}=z^2s_{ee})}{d\cos\theta^*}\bigg|_{\rm ave},\end{aligned}\tag{26}$$

where

$$\left.\frac{d\hat{\sigma}_{\lambda\lambda'}(\gamma\gamma\to hh;s_{\gamma\gamma})}{d\cos\theta^*}\right|_{\rm ave} \equiv \int_0^1 d\cos\theta^* \frac{d\hat{\sigma}_{\lambda\lambda'}(\gamma\gamma\to hh;s_{\gamma\gamma},\theta^*)}{d\cos\theta^*}, \quad (27)$$

$$\left[\frac{1}{L_{ee}}\frac{dL_{\gamma\gamma}}{dz}\left(\frac{1\pm\xi_2\xi_2'}{2}\right)\varepsilon_{\lambda\lambda'}\right](z) \equiv \int_{z^2/y_m}^{y_m} dy \int_0^1 d\cos\theta^* \frac{1}{L_{ee}}\frac{d^2L_{\gamma\gamma}}{dzdy}\left(\frac{1\pm\xi_2\xi_2'}{2}\right) \times \varepsilon_{\lambda\lambda'}(z,y,\theta^*). \quad (28)$$

Note that we approximate the differential cross section by its averaged value over $\cos\theta^*$. The total cut efficiency is estimated by generating event samples of isotropically produced Higgs pairs with the luminosity function, setting the c.m. energy of the Higgs pairs to $\sqrt{s_{\gamma\gamma}}$ and imposing all the selection cuts on the generated events.

Finally, we comment on our approximation that the Higgs pairs are produced isotropically. Using the maximum value of the differential cross section over the $\cos\theta^*$ range instead of the averaged one in Eq. (26), we obtain the upper bound of $\sigma_{\rm cut}$. We check that the differences between the upper bounds and our approximated cross section, Eq. (26), are less than 15%. This can be regarded as the uncertainty of our approximation, which is sufficient for our study as we will see in the next subsection.

2. $\gamma\gamma \to ZZ \to bb\bar{b}\bar{b}, b\bar{b}c\bar{c}$

Next, we discuss the ZZ background. The dominant background contributions are from $bb\bar{b}\bar{b}$ and $b\bar{b}c\bar{c}$ decay modes. Instead of directly estimating the ZZ background cross section with all the selection cuts being imposed ($\sigma_{\rm cut}$), we set an upper bound on the cross section by removing the preselection and S4 cuts since estimation of the efficiencies of those cuts needs more detailed simulation. The upper bound is written as

$$\begin{aligned}\sigma_{\rm cut}(\gamma\gamma\to ZZ\to bb\bar{b}\bar{b}, b\bar{b}c\bar{c};s_{ee}) &\lesssim \{{\rm Br}(Z\to b\bar{b})^2\varepsilon_{\rm S2}^{4b} + 2\,{\rm Br}(Z\to b\bar{b}) \times {\rm Br}(Z\to c\bar{c})\varepsilon_{\rm S2}^{2b2c}\}\varepsilon_{\rm S3} \\ &\times \sum_{\lambda\lambda'=++,+-}\int_{\sqrt{s_{\rm min}/s_{ee}}}^{\sqrt{s_{\rm max}/s_{ee}}} dz\left[\frac{1}{L_{ee}}\frac{dL_{\gamma\gamma}}{dz}\frac{1\pm\xi_2\xi_2'}{2}\right] \\ &\times (z)\hat{\sigma}_{\lambda\lambda'}(\gamma\gamma\to ZZ;s_{\gamma\gamma}=z^2s_{ee}), \end{aligned} \quad (29)$$

where $\varepsilon_{\rm S2}^{4b(2b2c)}$ and $\varepsilon_{\rm S3}$ are the efficiencies of the S2 cut for the $bb\bar{b}\bar{b}(b\bar{b}c\bar{c})$ decay mode and the S3 cut, respectively. In evaluating $\hat{\sigma}_{\lambda\lambda'}(\gamma\gamma\to ZZ;s_{\gamma\gamma})$, we use the one-loop expressions given in Ref. [24]. In Eq. (29), we approximately take into account the efficiencies of the S1, S2, and S3 cuts as follows. The effect of the S1 cut is approximated by limiting the integration interval, setting the upper and lower limits to those of the S1 cut, i.e., $\sqrt{s}_{\rm max} = m_\sigma + 40$ GeV and $\sqrt{s}_{\rm min} = m_\sigma - 60$ GeV for each sample model points. The efficiency of the S2 cut corresponds to the probability that three or four jets are b-tagged from the $bb\bar{b}\bar{b}$ ($b\bar{b}c\bar{c}$) final state and is obtained as $\varepsilon_{\rm S2}^{4b(2b2c)} \sim 0.82(0.12)$. The S3 cut efficiency is estimated from simulated event samples of Z boson pairs produced in the e^+e^- collision, setting the c.m. energy of the Z boson pair at m_σ since the peak region of the photon-photon luminosity is tuned at around this energy. This upper bound on the ZZ background will be used in estimating the upper bound on the total background in the next subsection.

TABLE II. The number of the signal and background events that pass all the selection cuts and the signal significance Z_0 with $\mathcal{L}_{ee} = 1$ ab^{-1} for each sample point.

	Point 1	Point 2	Point 3	Point 4
$m_{\tilde{t}_1}$ (GeV)	250	300	350	400
$\sigma(\gamma\gamma\to\sigma_{\tilde{t}_1}\to hh)$ (fb)	0.34	0.26	0.2	0.18
Signal	14.2	13.5	12.5	12.4
Total background	$\lesssim$3.9	$\lesssim$3.2	$\lesssim$2.3	$\lesssim$2.3
Nonresonant hh	2.2	2.1	1.7	1.4
$bb\bar{b}\bar{b}$	0.5	0.2	0.0	0.0
$c\bar{c}b\bar{b}$	0.4	0.5	0.2	0.1
ZZ	$\lesssim$0.8	$\lesssim$0.5	$\lesssim$0.3	$\lesssim$0.7
$t\bar{t}$	0.1	0.0	0.1	0.1
$cc\bar{c}\bar{c}$	0.0	0.0	0.0	0.0
$b\bar{b}q\bar{q}$	0.0	0.0	0.0	0.0
W^+W^-	0.0	0.0	0.0	0.0
W^+W^-Z	0.0	0.0	0.0	0.0
Significance Z_0	$\gtrsim$5.2	$\gtrsim$5.3	$\gtrsim$5.5	$\gtrsim$5.5

C. Results

We present expected signal and background event numbers with all the selection cuts imposed for the sample model points in Table II. Here, we assume the integrated electron-beam luminosity of 1 ab^{-1}. More than ten signal events are expected for all the sample points, while background events are effectively reduced to less than four events. We estimate the expected significance of detecting the $\sigma_{\tilde{t}_1}\to hh$ decay mode using an approximated formula based on the Poisson distribution [40],

$$Z_0 = \sqrt{2\{(S+B)\ln(1+S/B)-S\}}, \quad (30)$$

with S (B) being the expected signal (total background) event number.[6] The significance Z_0 for each sample point is also presented in Table II. Because we only estimate the upper bounds on the ZZ background, the expected significances are regarded as lower bounds. We see that for the

[6]This significance approaches to $S/\sqrt{B}$ when $S \ll B$.

TABLE III. The number of the signal and background events after the successive application of the cuts with $\mathcal{L}_{ee} = 1$ ab^{-1} for the sample Point 1. The efficiencies of each selection cut are also presented in parentheses. For the ZZ background, only an upper bound on the number of events that pass all the cuts is presented.

Point 1	Preselection + S1	+S2	+S3	+S4
Signal	32.8	26.8 (0.82)	18.0 (0.67)	14.2 (0.79)
Nonresonant hh	4.9	4.0 (0.82)	2.8 (0.70)	2.2 (0.76)
$bb\bar{b}\,\bar{b}$	42	34 (0.82)	1.9 (0.05)	0.5 (0.25)
$c\bar{c}b\bar{b}$	540	67 (0.12)	2.1 (0.03)	0.4 (0.17)
ZZ	-	-	-	$\lesssim$0.8
$t\bar{t}$	39	2.2 (0.06)	0.1 (0.04)	0.1 (1.00)
$cc\bar{c}\,\bar{c}$	1160	4.3 (0.004)	0.2 (0.04)	0.0 (0.17)
$b\bar{b}q\bar{q}$	1190	1.5 (0.001)	0.1 (0.04)	0.0 (0.25)
W^+W^-	195800	3.9 (2×10^{-5})	0.0 (0.00)	0.0 (0.00)
W^+W^-Z	5.0	0.2 (0.04)	0.0 (0.02)	0.0 (1.00)

5σ detection the signal cross sections, $\sigma(\gamma\gamma \to \sigma_{\tilde{t}_1} \to hh)$, of 0.34–0.18 fb are required for the stoponium masses of 500–800 GeV, respectively. In the rest of this section, we discuss how background events are reduced by imposing the selection cuts.

After imposing all the selection cuts, the major background source is the nonresonant Higgs pair (hh) production process, and the contributions from other background sources except $bb\bar{b}\,\bar{b}$, $b\bar{b}c\bar{c}$, and ZZ are negligibly small. We present the cut-flow information along with the cut efficiencies in parentheses for the sample Point 1 in Table III and for other points in Table IV, where only the non-negligible background processes are presented.

The selection cut S2, which requires three or four jets to be b-tagged, then plays an important role in reducing the large portion of the background events which needs some non-b jets to be mistagged to pass the cut.

The selection cut S3, relevant to the dijet invariant masses, also reduces most of the background events efficiently, except for nonresonant hh, by imposing Higgs mass constraints on two pairs of jets. At this stage, only the nonresonant hh, $bb\bar{b}\,\bar{b}$, $c\bar{c}b\bar{b}$, and ZZ backgrounds remain sizable.

The selection cut S4, which is based on ΔR distributions, further reduces the remaining $bb\bar{b}\,\bar{b}$ and $c\bar{c}b\bar{b}$ backgrounds. In Figs. 4, we present the $\min\{\Delta R_1, \Delta R_2\}$ and $\max\{\Delta R_1, \Delta R_2\}$ distributions of signal and $bb\bar{b}\,\bar{b}$ plus $c\bar{c}b\bar{b}$ background after imposing the preselection, S1, S2, and S3 cuts for the sample Point 1. We see that ΔR tends to be small for the signal, while it can be large up to $\sim$3 for the $bb\bar{b}\,\bar{b}$ plus $b\bar{b}c\bar{c}$ backgrounds. This difference makes the S4 cut efficient for reducing those backgrounds and can be understood qualitatively as follows. The dijet systems from the nonresonant multijet processes tend to distribute in the large $|\eta|$ region more than the dijet systems from decays of rather isotropically produced Higgs bosons. In general, two jets in a dijet system with larger $|\eta|$ tend to have a larger azimuthal angle difference, $\Delta\phi$, and thus larger ΔR; this mainly makes the difference in the ΔR distributions between the signal and the four-jet backgrounds above.

TABLE IV. Same as Table III but for the sample Points 2, 3, and 4, and only the non-negligible background processes are shown.

Point 2	Preselection + S1	+S2	+S3	+S4
Signal	28.6	23.4 (0.82)	14.6 (0.62)	13.5 (0.92)
Nonresonant hh	4.1	3.4 (0.82)	2.3 (0.67)	2.1 (0.93)
$bb\bar{b}\,\bar{b}$	30	25 (0.82)	0.3 (0.01)	0.2 (0.54)
$c\bar{c}b\bar{b}$	390	49 (0.12)	1.1 (0.02)	0.5 (0.43)
Point 3	Preselection + S1	+S2	+S3	+S4
Signal	23.2	19.0 (0.82)	12.9 (0.68)	12.5 (0.97)
Nonresonant hh	3.1	2.5 (0.82)	1.8 (0.70)	1.7 (0.97)
$bb\bar{b}\,\bar{b}$	24	19 (0.82)	0.1 (0.01)	0.0 (0.00)
$c\bar{c}b\bar{b}$	300	37 (0.12)	0.3 (0.01)	0.2 (0.50)
Point 4	Preselection + S1	+S2	+S3	+S4
Signal	21.6	17.7 (0.82)	12.6 (0.71)	12.4 (0.99)
Nonresonant hh	2.4	2.0 (0.82)	1.4 (0.71)	1.4 (0.99)
$bb\bar{b}\,\bar{b}$	17	14 (0.82)	0.1 (0.01)	0.0 (0.00)
$c\bar{c}b\bar{b}$	230	28 (0.12)	0.3 (0.01)	0.1 (0.50)

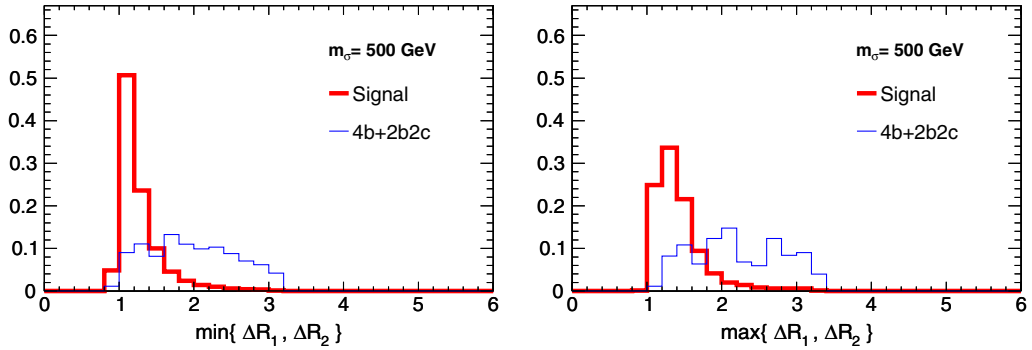

(a) $\min\{\Delta R_1, \Delta R_2\}$ (b) $\max\{\Delta R_1, \Delta R_2\}$

FIG. 4. The normalized distributions of $\min\{\Delta R_1, \Delta R_2\}$ (left) and $\max\{\Delta R_1, \Delta R_2\}$ (right) for Point 1 with all the cuts except S4 being imposed. The thick red lines are for the signal, and the thin blue lines are for the $bb\bar{b}\,\bar{b}$ plus $c\bar{c}b\bar{b}$.

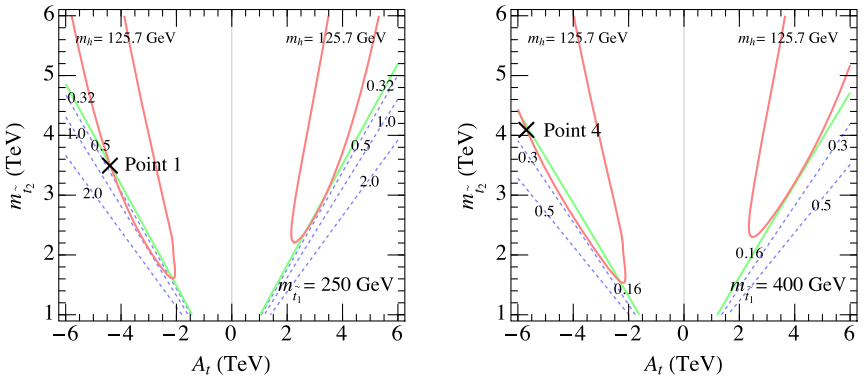

FIG. 5. The contours of the stoponium cross section, $\sigma(\gamma\gamma \to \sigma_{\tilde{t}_1} \to hh)$, and $m_h = 125.7$ GeV on the $m_{\tilde{t}_2}$–A_t plane for $m_{\tilde{t}_1} =$ 250 GeV (left) and 400 GeV (right). We take $m_{\tilde{\chi}_1^0} = 150$ GeV (left) and 350 GeV (right), $\tan\beta = 10$, $\mu = 2$ TeV and other SUSY parameters having dimension of mass equal to 2 TeV, except the trilinear couplings of the first and second generation sfermions which are set to zero. The dashed-blue lines show the cross sections, while the solid-green line represents the cross section which allows 5σ detection of the $\sigma_{\tilde{t}_1} \to hh$ mode. The contour labels are given in units of fb. The red curve shows the Higgs boson mass constraint. The sample model points in Sec. III are shown with the cross symbol.

IV. IMPLICATION TO THE STOP SECTOR

In the previous section, we have shown that there are possibilities to detect the di-Higgs decay mode of the stoponium and measure its cross section, $\sigma(\gamma\gamma \to \sigma_{\tilde{t}_1} \to hh)$. In this section, we discuss its implication for extracting information on the SUSY parameters in the stop sector: $m_{\tilde{t}_2}$ and A_t. Since we assume that the lighter stop and the lightest neutralino will be discovered by the time the photon-photon collider experiment will be carried out, their masses are regarded as known parameters. Some other SUSY parameters may also be known by that time, but we just assume them as unknown parameters for a conservative approach.

The heavier stop mass, $m_{\tilde{t}_2}$, and stop trilinear coupling, A_t, may be determined from the constraints of the measured cross section and Higgs mass up to the fourfold solutions when we fix the other SUSY parameters. This is illustrated in Fig. 5, where the four solutions appear on the $m_{\tilde{t}_2}$–A_t plane as the intersections between the contours of the stoponium cross section and Higgs mass.

Since we assume that the true SUSY parameter values are not known (except $m_{\tilde{t}_1}$ and $m_{\tilde{\chi}_1^0}$), we scan over the unknown SUSY parameters relevant to the stoponium cross sections and Higgs mass, finding possible solutions of $m_{\tilde{t}_2}$ and A_t in the parameter space. As an example result, we discuss upper bounds on $m_{\tilde{t}_2}$ and $|A_t|$.[7] For the paramter scan, we employ the phenomenological MSSM [41] as a SUSY framework. Besides $\tan\beta$ and μ parameters, which are relevant to the stoponium cross section and Higgs mass at tree level, the parameter space is spanned by the mass parameters of the sbottom, stau, and gluino: $M_{\tilde{b}_R}, M_{\tilde{\tau}_L}, M_{\tilde{\tau}_R}$, and M_3. For simplicity, we set $M_{\tilde{\tau}_L} = M_{\tilde{\tau}_R}$ and fix all the other SUSY mass parameters and trilinear couplings to 2 TeV. We check that the bounds are insensitive to these assumptions. In

[7]Lower bounds could also be derived in the same way; however, they depend on the uncertainty of the Higgs mass significantly, and we do not consider them in the following discussion.

TABLE V. The assumed SUSY parameter values and the ranges of the scanned parameters. The parentheses show the number of points taken for the corresponding parameter. The stoponium cross sections are set such that they allow 5σ detection of the $\gamma\gamma \to \sigma_{\tilde{t}_1} \to hh$ process. M_{others} represents the SUSY mass parameters which are not explicitly shown in the Table. $A_{\text{1st/2nd}}$ denotes the trilinear couplings related to the first and second generation sfermions.

$m_{\tilde{t}_1}$ [GeV]	250	300	350	400
$m_{\tilde{\chi}_1^0}$ [GeV]	150	250	300	350
$\sigma(\gamma\gamma \to \sigma_{\tilde{t}_1} \to hh)$ [fb]	0.34	0.26	0.2	0.18
$\tan\beta$	[10, 60] (3 points)			
μ	$[-10, 10]$ TeV (6 points)			
M_3	[2, 10] TeV (3 points)			
$M_{\tilde{b}_R}$	[2, 10] TeV (3 points)			
$M_{\tilde{\tau}_L} = M_{\tilde{\tau}_R}$	[2, 10] TeV (3 points)			
M_{others}	2 TeV			
$A_b = A_\tau$	2 TeV			
$A_{\text{1st/2nd}}$	2 TeV			

TABLE VI. The obtained upper bounds on $m_{\tilde{t}_2}$ and $|A_t|$ by the parameter scan for each $m_{\tilde{t}_1}$ value.

$m_{\tilde{t}_1}$ (GeV)	250	300	350	400
$m_{\tilde{t}_2}^{\text{upper}}$ (TeV)	3.8	4.2	4.6	4.7
$\lvert A_t\rvert^{\text{upper}}$ (TeV)	5.1	5.7	6.2	6.5

Table V, we summarize the scanned and assumed SUSY parameters for each $m_{\tilde{t}_1}$. We assume that the $\gamma\gamma \to \sigma_{\tilde{t}_1} \to hh$ process will be measured with more than 5σ significance and regard the cross sections given in Table II as the measured ones for each $m_{\tilde{t}_1}$. In obtaining bounds, we take into account statistical uncertainties of the signal measurements.

As shown in Table VI, the obtained upper bounds on $m_{\tilde{t}_2}$ and $|A_t|$ are 3.8–4.7 TeV and 5.1–6.5 TeV, respectively.[8] The upper bounds on $m_{\tilde{t}_2}$ are obtained well within the scanned parameter space and do not change significantly even if we extend the parameter space to $|\mu|, M_3, M_{\tilde{b}_R}, M_{\tilde{\tau}} < 14$ TeV from 10 TeV. On the other hand, the upper bounds on $|A_t|$ increase non-negligibly as we extend the parameter space; the dominant effects on the $|A_t|$ bounds are from the change of the μ parameter range since the A_t parameter linearly depends on the μ parameter through $A_t = X_t - \mu\cot\beta$. Thus, information on the μ parameter is important to obtain stringent bounds on A_t. As illustrated in this section, detection of the di-Higgs decay mode of the stoponium and measurement of its cross section would provide useful information on the stop sector.

[8]The upper bounds on $|A_t|$ are from the negative-large solutions, while the positive-large solutions also exist up to the similar, but ~1 TeV narrower, $|A_t|$ range.

V. SUMMARY AND CONCLUSION

In this study, we have investigated the detectability of the stoponium in the di-Higgs decay mode at the photon-photon collider. We have assumed that the lightest neutralino is the LSP, and the lighter stop is the next-to-lightest SUSY particle. We have also assumed that those particles would be discovered before the photon-photon collider experiment will be carried out and that the basic properties of the stop such as the mass and left-right mixing angle could be studied by that time. We have concentrated on the scenario where the mass difference between the stop and the neutralino is small enough, and the stop can form the stoponium.

The detectability of the stoponium di-Higgs decays has been investigated by estimating the stoponium signal and standard model backgrounds and optimizing the signal selection cuts. It has been found that 5σ detection of the di-Higgs decay mode is possible with the integrated electron-beam luminosity of 1 ab^{-1} if the signal cross sections, $\sigma(\gamma\gamma \to \sigma_{\tilde{t}_1} \to hh)$, of 0.34, 0.26, 0.2, and 0.18 fb are realized for the stoponium masses of 500, 600, 700, and 800 GeV, respectively. As concrete examples, we have provided the four sample model points in the MSSM, corresponding to those stoponium masses and realizing such cross sections.

Finally, we have discussed the implication of the cross section measurement of the stoponium di-Higgs decay mode for the MSSM stop sector. Combining the measured cross section with the Higgs-mass constraint, we have shown that there would be the upper bound on the heavier stop mass for each lighter stop and lightest neutralino masses. The A_t parameter would also be constrained, depending on other SUSY parameters such as μ and $\tan\beta$. In conclusion, there are possibilities that the di-Higgs decay mode of the stoponium would be observed unambiguously at the future photon-photon collider and provide new insights into the stop sector.

ACKNOWLEDGMENTS

The work is supported by Grant-in-Aid for Scientific research No. 23104008 and No. 26400239.

APPENDIX A: PHOTON LUMINOSITY FUNCTION

We use the luminosity function of the following form [19,20,23]:

$$\frac{1}{L_{ee}}\frac{d^2L_{\gamma\gamma}}{dydy'} = f(x,y)B(x,y)f(x,y')B(x,y'). \quad \text{(A1)}$$

The function f is given by

$$f(x,y) = \frac{2\pi\alpha_e^2}{\sigma_c x m_e^2} C_{00}(x,y), \tag{A2}$$

where the function C_{00} is given in Eq. (14) and

$$\sigma_c = \sigma_c^{(\mathrm{np})} + \lambda_e P_l \sigma_1, \tag{A3}$$

with

$$\sigma_c^{(\mathrm{np})} = \frac{2\pi\alpha_e^2}{x m_e^2}\left[\left(1-\frac{4}{x}-\frac{8}{x^2}\right)\ln(x+1)+\frac{1}{2}+\frac{8}{x}-\frac{1}{2(x+1)^2}\right], \tag{A4}$$

$$\sigma_1 = \frac{2\pi\alpha_e^2}{x m_e^2}\left[\left(1+\frac{2}{x}\right)\ln(x+1)-\frac{5}{2}+\frac{1}{x+1}-\frac{1}{2(x+1)^2}\right]. \tag{A5}$$

The function B is given by

$$B(x,y) = \begin{cases} \exp\left[-\frac{\rho^2}{8}\left(\frac{x}{y}-x-1\right)\right] & : y_m/2 < y < y_m \\ 0 & : \text{otherwise} \end{cases}, \tag{A6}$$

with $y_m = x/(x+1)$. In our numerical calculation, we take $\rho = 1$ [23].

APPENDIX B: MATRIX ELEMENTS

We summarize the matrix elements for the stop-antistop annihilation processes used in our study [6,9]. We assume that all the SUSY particles, except the stops, sbottoms, and lightest neutralino, are sufficiently heavy and neglect their contributions. We also assume that the lightest neutralino is purely binolike. In the following expressions, the summations over the color indices of the initial stop and antistop have been implicitly performed as

$$|\mathcal{M}(\tilde{t}_1\tilde{t}_1^* \to AB)|^2 = \left|\frac{1}{3}\sum\nolimits_a \mathcal{M}(\tilde{t}_1^a\tilde{t}_1^{a*} \to AB)\right|^2, \tag{B1}$$

and the explicit color summations should be taken for the final-state colored paricles.

1. gg

In the $v = 0$ limit (where v is the velocity of the stops in the initial state), the contributions from the t- and u-channel stop exchanges are absent. Therefore, the squared matrix element does not depend on the MSSM parameters and is given by

$$\sum_{\text{color, helicity}} |\mathcal{M}(\tilde{t}_1\tilde{t}_1^* \to gg)|^2_{v=0} = \left(\frac{16\pi}{3}\alpha_s\right)^2. \tag{B2}$$

2. $\gamma\gamma$

As in the gg final-state case, the squared matrix element for the $\gamma\gamma$ final state does not depend on the MSSM parameters and is given by

$$\sum_{\text{helicity}} |\mathcal{M}(\tilde{t}_1\tilde{t}_1^* \to \gamma\gamma)|^2_{v=0} = 128\pi^2\left(\frac{2}{3}\right)^4\alpha_e^2. \tag{B3}$$

3. hh

The squared matrix element is given by

$$|\mathcal{M}(\tilde{t}_1\tilde{t}_1^* \to hh)|^2_{v=0} = \left\{\frac{2(c^{(2)}_{\tilde{t}_1})^2}{2m^2_{\tilde{t}_1}-m_h^2}+\frac{2(c^{(2)}_{\tilde{t}_1\tilde{t}_2})^2}{m^2_{\tilde{t}_1}+m^2_{\tilde{t}_2}-m_h^2}+c_{11}^{22} + \frac{c^{(2)}_{\tilde{t}_1}}{4m^2_{\tilde{t}_1}-m_h^2}\frac{3gm_Z}{2c_W}\cos 2\alpha\sin(\beta+\alpha)\right\}^2, \tag{B4}$$

where g is the $SU(2)_L$ gauge coupling constant, $c_W = \cos\theta_W$, $s_W = \sin\theta_W$, and α is the mixing angle of the CP-even Higgs bosons. In addition, $c^{(2)}_{\tilde{t}_1}$, $c^{(2)}_{\tilde{t}_1\tilde{t}_2}$, and c_{11}^{22} are the coefficients of the $\tilde{t}_1\tilde{t}_1^*h$, $\tilde{t}_1\tilde{t}_2^*h$, and $\tilde{t}_1\tilde{t}_1^*hh$ vertices, respectively, and are given by

$$c^{(2)}_{\tilde{t}_1} = \frac{gm_Z}{c_W}\sin(\alpha+\beta)\left(\frac{1}{2}\cos^2\theta_{\tilde{t}}-\frac{2}{3}s_W^2\cos 2\theta_{\tilde{t}}\right) - \frac{gm_t^2}{m_W}\frac{\cos\alpha}{\sin\beta}+\frac{gm_t}{2m_W\sin\beta}\sin 2\theta_{\tilde{t}}(A_t\cos\alpha-\mu\sin\alpha), \tag{B5}$$

$$c^{(2)}_{\tilde{t}_1\tilde{t}_2} = \frac{gm_Z}{c_W}\sin(\alpha+\beta)\sin 2\theta_{\tilde{t}}\left(\frac{2}{3}s_W^2-\frac{1}{4}\right) + \frac{gm_t}{2m_W\sin\beta}\cos 2\theta_{\tilde{t}}(A_t\cos\alpha-\mu\sin\alpha), \tag{B6}$$

$$c_{11}^{22} = \frac{g^2}{2}\left[\frac{\cos 2\alpha}{c_W^2}\left(\frac{1}{2}\cos^2\theta_{\tilde{t}}-\frac{2}{3}s_W^2\cos 2\theta_{\tilde{t}}\right)-\frac{m_t^2}{m_W^2}\frac{\cos^2\alpha}{\sin^2\beta}\right]. \tag{B7}$$

4. W^+W^-

The squared matrix element is given by

$$\sum_{\text{spin}}|\mathcal{M}(\tilde{t}_1\tilde{t}_1^* \to W^+W^-)|^2_{v=0} = 2(a^T_{WW})^2+(a^L_{WW})^2, \tag{B8}$$

where a^T_{WW} and a^L_{WW} correspond to the transverse and longitudinal components of the matrix element and are given by

$$a_{WW}^{T} = \mathcal{M}^{+1+1} = \mathcal{M}^{-1-1} = -\left(\frac{g^2}{2}\cos^2\theta_{\tilde{t}} - \frac{g_{hWW}c_{\tilde{t}_1}^{(2)}}{4m_{\tilde{t}_1}^2 - m_h^2}\right) \tag{B9}$$

and

$$a_{WW}^{L} = \mathcal{M}^{00} = \left(\frac{2m_{\tilde{t}_1}^2}{m_W^2} - 1\right)\left(\frac{g^2}{2}\cos^2\theta_{\tilde{t}} - \frac{g_{hWW}c_{\tilde{t}_1}^{(2)}}{4m_{\tilde{t}_1}^2 - m_h^2}\right) - 2\left(\frac{m_{\tilde{t}_1}^2}{m_W^2} - 1\right)\left(\frac{g^2\cos^2\theta_{\tilde{t}}m_{\tilde{t}_1}^2}{m_{\tilde{t}_1}^2 + m_{\tilde{b}_L}^2 - m_W^2}\right), \tag{B10}$$

respectively. Here, $m_{\tilde{b}_L}$ is the left-handed sbottom mass (where we neglect the left-right sbottom mixing), and g_{hWW} is the coefficient of the hW^+W^- vertex, which is given by

$$g_{hWW} = gm_W \sin(\beta - \alpha). \tag{B11}$$

Note that in the $v \to 0$ limit the contribution of the s-channel Z boson exchange is absent.

5. ZZ

The squared matrix element is given by

$$\sum_{\text{spin}} |\mathcal{M}(\tilde{t}_1\tilde{t}_1^* \to ZZ)|_{v=0}^2 = 2(a_{ZZ}^{T})^2 + (a_{ZZ}^{L})^2, \tag{B12}$$

where

$$a_{ZZ}^{T} = \mathcal{M}^{+1+1} = \mathcal{M}^{-1-1} = \frac{1}{c_W^2}\left[2g^2\left\{\left(\frac{1}{4} - \frac{2}{3}s_W^2\right)\cos^2\theta_{\tilde{t}} + \frac{4}{9}s_W^4\right\} - \frac{g_{hWW}c_{\tilde{t}_1}^{(2)}}{4m_{\tilde{t}_1}^2 - m_h^2}\right] \tag{B13}$$

and

$$a_{ZZ}^{L} = \mathcal{M}^{00} = -\frac{1}{c_W^2}\left(\frac{2m_{\tilde{t}_1}^2}{m_Z^2} - 1\right)\left[2g^2\left\{\left(\frac{1}{4} - \frac{2}{3}s_W^2\right)\cos^2\theta_{\tilde{t}} + \frac{4}{9}s_W^4\right\} - \frac{g_{hWW}c_{\tilde{t}_1}^{(2)}}{4m_{\tilde{t}_1}^2 - m_h^2}\right] + \frac{2g^2m_{\tilde{t}_1}^2}{c_W^2}\left(\frac{m_{\tilde{t}_1}^2}{m_Z^2} - 1\right) \times \left[\frac{(\cos^2\theta_{\tilde{t}} - \frac{4}{3}s_W^2)^2}{2m_{\tilde{t}_1}^2 - m_Z^2} + \frac{\cos^2\theta_{\tilde{t}}\sin^2\theta_{\tilde{t}}}{m_{\tilde{t}_1}^2 + m_{\tilde{t}_2}^2 - m_Z^2}\right]. \tag{B14}$$

6. Zγ

The squared matrix element is given by

$$\sum_{\text{spin, helicity}} |\mathcal{M}(\tilde{t}_1\tilde{t}_1^* \to Z\gamma)|_{v=0}^2 = 8\left(\frac{2}{3}\right)^2 g^2g'^2\left(\frac{1}{2}\cos^2\theta_{\tilde{t}} - \frac{2}{3}s_W^2\right)^2, \tag{B15}$$

where g' is the hypercharge gauge coupling constant.

7. $b\bar{b}$

The squared matrix element is given by

$$\sum_{\text{color,spin}} |\mathcal{M}(\tilde{t}_1\tilde{t}_1^* \to b\bar{b})|_{v=0}^2 = 24(m_{\tilde{t}_1}^2 - m_b^2)\left(\frac{gm_b}{2m_W}\frac{\sin\alpha}{\cos\beta}\frac{c_{\tilde{t}_1}^{(2)}}{4m_{\tilde{t}_1}^2 - m_h^2}\right)^2. \tag{B16}$$

8. $t\bar{t}$

The squared matrix element is given by

$$\sum_{\text{color,spin}} |\mathcal{M}(\tilde{t}_1\tilde{t}_1^* \to t\bar{t})|_{v=0}^2 = 24(m_{\tilde{t}_1}^2 - m_t^2)\left\{\frac{1}{3}\frac{m_{\tilde{\chi}_1^0}(a_1^2 - b_1^2) + m_t(a_1^2 + b_1^2)}{m_t^2 - m_{\tilde{t}_1}^2 - m_{\tilde{\chi}_1^0}^2} - \frac{gm_t}{2m_W}\frac{\cos\alpha}{\sin\beta}\frac{c_{\tilde{t}_1}^{(2)}}{4m_{\tilde{t}_1}^2 - m_h^2}\right\}^2, \tag{B17}$$

where

$$a_1 = -\frac{1}{\sqrt{2}}g'\left(\frac{1}{6}\cos\theta_{\tilde{t}} - \frac{2}{3}\sin\theta_{\tilde{t}}\right), \tag{B18}$$

$$b_1 = -\frac{1}{\sqrt{2}}g'\left(\frac{1}{6}\cos\theta_{\tilde{t}} + \frac{2}{3}\sin\theta_{\tilde{t}}\right). \tag{B19}$$

9. $\tilde{\chi}_1^0\tilde{\chi}_1^0$

The squared matrix element is given by

$$\sum_{\text{spin}} |\mathcal{M}(\tilde{t}_1\tilde{t}_1^* \to \tilde{\chi}_1^0\tilde{\chi}_1^0)|_{v=0}^2 = 8(m_{\tilde{t}_1}^2 - m_{\tilde{\chi}_1^0}^2)\left\{\frac{2m_t(a_1^2 - b_1^2) + 2m_{\tilde{\chi}_1^0}(a_1^2 - b_1^2)}{m_{\tilde{\chi}_1^0}^2 - m_{\tilde{t}_1}^2 - m_t^2}\right\}^2. \tag{B20}$$

[1] D. S. Gorbunov and V. A. Ilyin, J. High Energy Phys. 11 (2000) 011.
[2] D. S. Gorbunov, V. A. Ilyin, and V. I. Telnov, Nucl. Instrum. Methods Phys. Res., Sect. A **472**, 171 (2001).
[3] M. J. Herrero, A. Mendez, and T. G. Rizzo, Phys. Lett. B **200**, 205 (1988).
[4] V. D. Barger and W. Y. Keung, Phys. Lett. B **211**, 355 (1988).
[5] H. Inazawa and T. Morii, Phys. Rev. Lett. **70**, 2992 (1993).
[6] M. Drees and M. M. Nojiri, Phys. Rev. D **49**, 4595 (1994).
[7] M. Drees and M. M. Nojiri, Phys. Rev. Lett. **72**, 2324 (1994).
[8] M. Antonelli and N. Fabiano, Eur. Phys. J. C **16**, 361 (2000).
[9] S. P. Martin, Phys. Rev. D **77**, 075002 (2008).
[10] S. P. Martin and J. E. Younkin, Phys. Rev. D **80**, 035026 (2009).
[11] Y. Kats and M. D. Schwartz, J. High Energy Phys. 04 (2010) 016.
[12] J. E. Younkin and S. P. Martin, Phys. Rev. D **81**, 055006 (2010).
[13] D. Kahawala and Y. Kats, J. High Energy Phys. 09 (2011) 099.
[14] V. Barger, M. Ishida, and W.-Y. Keung, Phys. Rev. Lett. **108**, 081804 (2012).
[15] Y. Kats and M. J. Strassler, J. High Energy Phys. 11 (2012) 097.
[16] C. Kim, A. Idilbi, T. Mehen, and Y. W. Yoon, Phys. Rev. D **89**, 075010 (2014).
[17] N. Kumar and S. P. Martin, Phys. Rev. D **90**, 055007 (2014).
[18] B. Batell and S. Jung, J. High Energy Phys. 07 (2015) 061.
[19] I. F. Ginzburg, G. L. Kotkin, V. G. Serbo, and V. I. Telnov, Nucl. Instrum. Methods Phys. Res. **205**, 47 (1983).
[20] I. F. Ginzburg, G. L. Kotkin, S. L. Panfil, V. G. Serbo, and V. I. Telnov, Nucl. Instrum. Methods Phys. Res., Sect. A **219**, 5 (1984).
[21] T. Behnke *et al.*, arXiv:1306.6327.
[22] K. Hagiwara, K. Kato, A. D. Martin, and C. K. Ng, Nucl. Phys. **B344**, 1 (1990).
[23] I. F. Ginzburg and G. L. Kotkin, Eur. Phys. J. C **13**, 295 (2000).
[24] G. J. Gounaris, J. Layssac, P. I. Porfyriadis, and F. M. Renard, Eur. Phys. J. C **13**, 79 (2000).
[25] S. Heinemeyer, W. Hollik, and G. Weiglein, Comput. Phys. Commun. **124**, 76 (2000).
[26] S. Heinemeyer, W. Hollik, and G. Weiglein, Eur. Phys. J. C **9**, 343 (1999).
[27] G. Degrassi, S. Heinemeyer, W. Hollik, P. Slavich, and G. Weiglein, Eur. Phys. J. C **28**, 133 (2003).
[28] M. Frank, T. Hahn, S. Heinemeyer, W. Hollik, H. Rzehak, and G. Weiglein, J. High Energy Phys. 02 (2007) 047.
[29] T. Hahn, S. Heinemeyer, W. Hollik, H. Rzehak, and G. Weiglein, Phys. Rev. Lett. **112**, 141801 (2014).
[30] N. Fabiano, A. Grau, and G. Pancheri, Phys. Rev. D **50**, 3173 (1994).
[31] N. Fabiano and O. Panella, Phys. Rev. D **72**, 015005 (2005); **72**, 019902(E) (2005).
[32] N. Fabiano and O. Panella, Phys. Rev. D **81**, 115001 (2010).
[33] J. Alwall, R. Frederix, S. Frixione, V. Hirschi, F. Maltoni, O. Mattelaer, H.-S. Shao, T. Stelzer, P. Torrielli, and M. Zaro, J. High Energy Phys. 07 (2014) 079.
[34] T. Sjostrand, S. Mrenna, and P. Z. Skands, J. High Energy Phys. 05 (2006) 026.
[35] J. de Favereau, C. Delaere, P. Demin, A. Giammanco, V. Lemaître, A. Mertens, and M. Selvaggi (DELPHES 3 Collaboration), J. High Energy Phys. 02 (2014) 057.
[36] T. Behnke *et al.*, arXiv:1306.6329.
[37] M. Cacciari, G. P. Salam, and G. Soyez, Eur. Phys. J. C **72**, 1896 (2012); M. Cacciari and G. P. Salam, Phys. Lett. B **641**, 57 (2006).
[38] M. Cacciari, G. P. Salam, and G. Soyez, J. High Energy Phys. 04 (2008) 063.
[39] G. V. Jikia, Nucl. Phys. **B412**, 57 (1994).
[40] G. Cowan, K. Cranmer, E. Gross, and O. Vitells, Eur. Phys. J. C **71**, 1554 (2011); **73**, 2501 (2013).
[41] C. F. Berger, J. S. Gainer, J. L. Hewett, and T. G. Rizzo, J. High Energy Phys. 02 (2009) 023.